https://doi.org/10.5194/egusphere-2026-778
Preprint. Discussion started: 17 February 2026

Nonlinear dynamics of time-variable slope circulation

Anna Lina Petruseviciute Sjur[1], Pål Erik Isachsen[1,2], Johan Nilsson[3], and Susan Allen[4]

[1]Department of Geosciences, University of Oslo, Oslo, Norway
[2]Ocean Department, Norwegian Meteorological Institute, Oslo, Norway
[3]Department of Meteorology, Stockholm University, Stockholm, Sweden
[4]Department of Earth, Ocean and Atmospheric Sciences, University of British Columbia, Vancouver, Canada

Correspondence: Anna Lina Petruseviciute Sjur (a.l.p.sjur@geo.uio.no)

Abstract. Bottom topography strongly constrains ocean circulation in the Arctic, and both theory and numerical modeling suggest that nonlinear flow–topography interactions influence slope-following currents. Yet, how such interactions modify the circulation response to time-variable surface forcing remains poorly understood. Using idealized shallow-water simulations of flow over a corrugated slope in a re-entrant channel, we investigate how nonlinear features arise and evolve under oscillatory forcing. We observe both a persistent prograde flow bias (aligned with topographic Rossby wave propagation) relative to linear estimates, and an asymmetry in the circulation response, with retrograde flow (opposing wave propagation) exhibiting a saturation of flow strength once the flow reaches sufficiently strong velocities. To identify the mechanisms responsible for these behaviors, we evaluate integrated momentum budgets. Which terms appear as dynamically relevant, in addition to linear surface and bottom stresses, depends on the choice of integration path: when integrated along constant-depth contours, the nonlinear dynamics appear as a cross-slope relative vorticity flux, whereas integration along straight transects instead highlights momentum flux convergence and topographic form stress. These perspectives can be unified under quasi-geostrophic scaling as describing a flux of potential vorticity (PV). This PV flux is strongest during retrograde flow and predominantly downslope, explaining the prograde bias. When retrograde velocities approach the arrest speed of topographic Rossby waves with wavelengths comparable to the corrugation scale, the flux increases sharply, halting further acceleration and producing the observed asymmetry. These results show how flow–topography interactions shape time-variable slope circulation, biasing the flow toward prograde states and limiting retrograde flow strength. Such effects are likely underrepresented in coarse-resolution numerical simulations, and highlight the need for improved representations of unresolved topographic interactions.

1 Introduction

The large-scale time-mean circulation of the Arctic Ocean is strongly topographically steered (Nøst and Isachsen, 2003; Yang et al., 2016; Broomé and Nilsson, 2016; Nilsson et al., 2024), with boundary currents closely following the continental slopes and ridges (e.g. Woodgate et al., 2001; Kallmyr et al., 2025). These boundary currents are a crucial component of Arctic Ocean circulation: they carry and redistribute the warm, saline Atlantic Water that enters the Arctic Ocean, thereby influencing sea-ice cover, water-mass transformation, and the export of modified waters back to the North Atlantic (e.g. Timmermans and Marshall, 2020; Woodgate, 2013). However, despite their central role in Arctic Ocean circulation, the dynamics governing

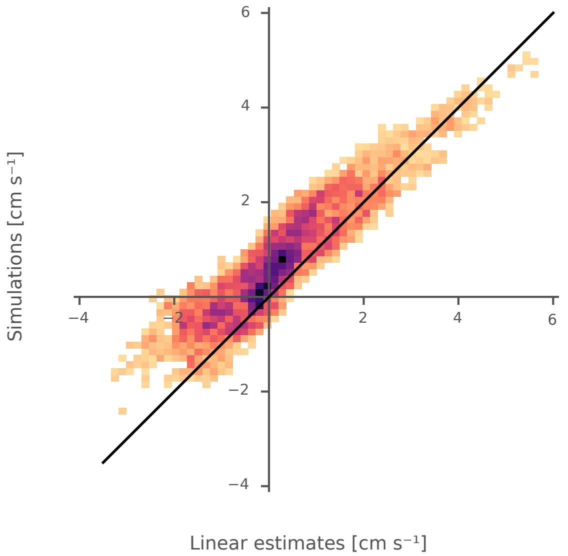

Figure 1. Two-dimensional histogram of normalized Arctic Ocean circulation around depth contours in several subbasins from a linear, idealized model versus realistic, numerical simulations. Data density increases with darker shading.The data falls parallel to the 1–1 line (black), indicating strong correlation, but is systematically shifted upward, revealing a cyclonic bias. Deviations are largest for negative (anticyclonic) circulation values, hinting at a directional asymmetry in the agreement with linear theory. Adapted with permission from Sjur et al. (2025).

slope-following boundary currents, including the contribution of nonlinear flow–topography interactions, remain incompletely understood.

This study is motivated by fundamental questions on flow–topography interactions, which were highlighted in recent analyses of a realistic Arctic Ocean simulation presented by Sjur et al. (2025). They examined an eddy-permitting, 4 km resolution baroclinic ocean-circulation model configuration (ROMS) that spans the Nordic Seas and Arctic Ocean and is coupled to a sea-ice model. It captures the major slope-following currents and provides daily output for 2014–2019. In these simulations, time-variable basin circulation around closed depth contours was strongly correlated with estimates from simplified linear theory (Fig. 1). In this simplified theory, first developed in Isachsen et al. (2003), the time evolution of circulation around closed f/H-contours (corresponding to depth contours under the f-plane approximation) is governed solely by surface stress and a linear bottom drag, yielding an estimate of circulation as a low-pass filtered and lagged response to surface forcing. The close agreement between linear theory and realistic numerical simulations thus suggested that much of the model simulated Arctic Ocean response to variable surface stress can be understood using linear dynamics.

However, two deviations from linear theory emerged from this analysis, as seen in Fig. 1. Specifically,

1. the numerical model circulation exhibited a systematically more cyclonic response than predicted by linear theory, and

2. the deviations were larger for retrograde than for prograde forcing, indicating a directional asymmetry in the response.

Here, the prograde direction aligns with topographic Rossby wave propagation and corresponds to cyclonic circulation in a basin, whereas retrograde opposes it and corresponds to anticyclonic circulation.

While these deviations were relatively modest in the pan-Arctic simulations studied in Sjur et al. (2025), similar analyses of Argo float observations from the Lofoten Basin in the Nordic Seas revealed cyclonic flow along the isobath that was nearly twice as strong as the flow obtained from the linear model, when forced with observed winds (Johnston et al., 2025). In the same study, analysis of a high-resolution simulation of the region linked the offset to an eddy-driven flux of relative vorticity into the basin, which, by Gauss's theorem, implies a net cyclonic tendency. These simulations were substantially higher in resolution (800 m) than those analyzed in Sjur et al. (2025), and the cyclonic offset for the same region was also more pronounced. Together, these findings suggest that nonlinear interactions drive a cyclonic tendency, and that the effect is particularly pronounced in eddy-active regions such as the Lofoten Basin. The stronger offset in the higher-resolution simulation further indicates that resolving mesoscale eddies is essential for capturing this effect.

This persistent bias towards cyclonic flow in basins is consistent with theoretical models predicting that eddies interacting with topography drive the flow toward a state aligned, in a prograde sense, with the underlying bathymetry – a tendency often referred to as the "Neptune effect" (Holloway, 1996). In particular, the minimum potential enstrophy state described by Bretherton and Haidvogel (1976) and the maximum entropy framework of Salmon et al. (1976) both predict the end state of freely evolving, decaying turbulence as anticyclones over bumps and cyclonic gyres in basins. It is worth noting, however, that these theories do not account for external forcing or the mechanisms by which the system reaches this state. In the Lofoten Basin simulations in Johnston et al. (2025), the mechanism was explicitly diagnosed as the eddy-driven relative-vorticity flux into the basin, as introduced above.

The Lofoten study discussed above considers a regime with mainly cyclonic wind forcing, and therefore could not shed light on the second feature, namely a directional asymmetry. A systematically weaker response of slope-currents to retrograde forcing is, however, consistent with literature linking such asymmetries to topographic form stress (e.g. Brink, 1986), which is the net pressure force exerted by the flow against topographic irregularities. Topographic form stress is typically stronger for retrograde flow (see i.e., Bai et al., 2021, for an idealized study of how topographic form stress depends on the forcing direction). While form stress itself is linear in the equations of motion, asymmetries in its magnitude can arise from nonlinear flow–topography interactions. In particular, when retrograde flow becomes strong enough to arrest Rossby waves matching the dominant wavelength of the underlying topography (recall that retrograde flow opposes Rossby wave propagation), the resulting large-amplitude pressure gradients across topographic features considerably enhance the form stress. As an example, topographic form stress has been shown to nearly balance the surface wind stress along the Antarctic Circumpolar Current, where the eastward flow arrests planetary Rossby waves (e.g., Munk and Palmén, 1951; Stevens and Ivchenko, 1997; Ward and Hogg, 2011; Stewart and Hogg, 2017; Masich et al., 2015). In the Arctic, by contrast, the steep continental slopes and strongly steered boundary currents suggest that the relevant mechanism is the arrest of *topographic* Rossby waves. Nevertheless, the overall contribution of topographic form stress to the Arctic momentum balance remains poorly understood.

The ocean surface stress in the Arctic is determined by surface winds and sea-ice cover, and it exhibits strong short-term synoptic fluctuations superimposed on a seasonal cycle (see e.g., Fig. 5 in Sjur et al., 2025). This highly variably surface stress highlights the need to examine the effect of nonlinearities under time-dependent forcing. Nevertheless, studies using steady wind forcing can offer some insight into the mechanisms causing the asymmetry between prograde and retrograde flows. Notably, Holloway (1987) presented a series of steady-state simulations of flow over topography, spanning a range of forcing strengths in both the prograde and retrograde direction. These simulations reproduced both a cyclonic offset and a directional asymmetry in flow strength, closely resembling the nonlinear features found by Sjur et al. (2025). Further, he argued that topographic form stress provides the physical mechanism underlying both features.

A few studies have explored the role of topographic form stress under time-variable forcing. Haidvogel and Brink (1986) showed that barotropic flow over corrugated slopes, driven by an oscillatory along-slope surface stress with a mean value of zero, develops a time-mean residual prograde circulation. This result can be interpreted via the domain and time-integrated momentum balance: while the surface stress is directionally symmetric, the topographic form stress responds asymmetrically, exerting greater stress during retrograde phases. This asymmetry is balanced by a stronger bottom frictional stress, and thus a stronger flow, in the prograde phase, giving rise to a residual prograde circulation. Similar results of a residual prograde flow have been derived from quasi-geostrophic theory (Samelson and Allen, 1987) and observed in laboratory tank experiments (e.g., Zhang et al., 1996; Boyer et al., 2000). Brink (2010) conducted related numerical experiments, and proposed a parametrization for the residual flow as a function of across-isobath velocity perturbations.

Building on the ideas introduced above, we seek to understand the deviations from linear theory suggested by the realistic simulation analyzed by Sjur et al. (2025), in particular the persistent prograde offset and the asymmetric response to prograde and retrograde forcing. To examine these deviations, we analyze how nonlinear contributions evolve under oscillating forcing in a set of idealized shallow-water simulations. This time-dependent perspective separates the two signatures of nonlinearity that would otherwise merge in time-mean analyses, where a time dependent asymmetry would average to a mean offset. We also examine how the response depends on the forcing period, reflecting the broad range of surface stress variability in the Arctic Ocean. Moreover, because explanations for departures from linear theory have mainly emphasized either form stress asymmetry or eddy-mediated vorticity fluxes, we make an effort to reconcile these perspectives by applying both diagnostics to the same system. Specifically, we ask:

1. How do nonlinearities and flow–topography interactions modify the relationship between surface forcing and circulation?
2. To what extent does the forcing period control whether the system exhibits a persistent offset or an asymmetric response?
3. How do two complementary diagnostic perspectives – one based on straight transects and the other on depth-following contours, in which topographic form stress and vorticity fluxes play distinct roles – capture and jointly explain these nonlinear effects?

The rest of the paper is organized as follows; in Section 2 we introduce the model configuration and forcing setup. In Section 3 we present the two momentum-budget frameworks and theoretical considerations that guide their interpretation, as

https://doi.org/10.5194/egusphere-2026-778
Preprint. Discussion started: 17 February 2026

well as an unifying PV perspective. In Section 4, we first compare linear estimates and simulations, paralleling the analysis behind Fig. 1, before presenting analyses in both momentum-budget frameworks. Further, we examine whether arrested-wave theory can explain the observed asymmetry. We also consider a case without corrugations, to further isolate the contribution of flow–topography interactions. In Section 5, we discuss how our findings from this idealized study applies to more realistic settings, together with consequences for modeling, before we conclude in Section 6, by returning to questions 1-3 above.

2 Numerical model

To idealize topographically steered flow under time-variable forcing, we preform a series of shallow water simulations of flow over a slope with a forcing varying sinusoidally in time. The idealized setup is similar to the approach in earlier studies (Brink, 2010; Haidvogel and Brink, 1986). Simulations are implemented using the Oceananigans.jl software package (Wagner et al., 2025). The full model configuration files can be found in [add reference to zenodo, once code is published]

2.1 Governing equations

The shallow water equations describe the flow of a single-layer fluid with constant density, where velocity varies only in the horizontal plane. The horizontal velocity vector is given by $\boldsymbol{u} = u\boldsymbol{i} + v\boldsymbol{j}$, and the total fluid depth is $D = H + \eta$, where $H(x,y)$ is the fluid depth at rest and $\eta(x,y,t)$ is the free surface elevation. Unit vectors in the x, y and z directions are written as $\boldsymbol{i}$, $\boldsymbol{j}$ and $\boldsymbol{k}$. The governing equations are

$$\partial_t (D\boldsymbol{u}) + \boldsymbol{\nabla} \cdot (D\boldsymbol{u}\boldsymbol{u}) + f\boldsymbol{k} \times (D\boldsymbol{u}) = -D\boldsymbol{\nabla}\phi + \boldsymbol{\tau}_s - \boldsymbol{\tau}_b \tag{1}$$

and

$$\partial_t D + \boldsymbol{\nabla} \cdot (D\boldsymbol{u}) = 0, \tag{2}$$

where f is the Coriolis parameter, and $\boldsymbol{\tau}_s$ and $\boldsymbol{\tau}_b$ are the surface and bottom kinematic stresses, respectively. Additionally, $\phi = g\eta$ is the dynamic pressure, where g is the gravitational acceleration. A derivative with respect to a variable x is written on the form ∂_x, so that ∂_t is a time derivative.

Depending on the diagnostic purpose, it can be convenient to rewrite the momentum equation in its vector-invariant form. Using the identity

$$\boldsymbol{u} \cdot \nabla \boldsymbol{u} = \zeta \boldsymbol{k} \times \boldsymbol{u} + \frac{1}{2} \nabla (\boldsymbol{u} \cdot \boldsymbol{u}), \tag{3}$$

where

$$\zeta = \partial_x v - \partial_y u \tag{4}$$

is the relative vorticity, we can rewrite Eq. (1) as

$$D\partial_t \boldsymbol{u} + D(\zeta + f)\boldsymbol{k} \times \boldsymbol{u} = -D\boldsymbol{\nabla}\left[\phi + \frac{1}{2}(\boldsymbol{u} \cdot \boldsymbol{u})\right] + \boldsymbol{\tau}_s - \boldsymbol{\tau}_b. \tag{5}$$

https://doi.org/10.5194/egusphere-2026-778
Preprint. Discussion started: 17 February 2026

As we will come back to, this formulation highlights the explicit role of vorticity fluxes.

We further assume a constant Coriolis parameter $f = 10^{-4}\mathrm{s}^{-1}$, appropriate for high-latitude regions where variations in planetary vorticity are small. The bottom stress is modeled as a linear drag,

$$\boldsymbol{\tau}_b = R\boldsymbol{u}, \tag{6}$$

where $R = 5\times10^{-4}\,\mathrm{m\,s^{-1}}$ is a constant bottom drag coefficient. This value is chosen based on typical values diagnosed in Sjur et al. (2025).

2.2 Domain geometry

We consider an idealized horizontal domain with extents of $L_x = L_y = 90\,\mathrm{km}$, discretized using a uniform grid with resolution $\Delta x = \Delta y = 1\,\mathrm{km}$. The domain is periodic in the x-direction, and bounded by solid, no-flux walls at $y = 0$ and $y = L_y$. This configuration permits continuous circulation in the x-direction, analogous to a slope current around a basin.

The bottom topography consists of a slope independent of x, with a smooth transition from a shallow shelf to a deeper basin as y increases. Superimposed are along-slope sinusoidal corrugations, scaled with the local steepness. The bathymetry is given by $H(x,y)$, and is defined as

$$H(x,y) = H_{\mathrm{sh}} + \frac{1}{2}(H_{\mathrm{bs}} - H_{\mathrm{sh}})\left[1 + \tanh\left(\frac{\pi(y - y_c - \delta(x,y))}{W}\right)\right] \tag{7}$$

where the corrugation displacement $\delta(x,y)$ is specified as

$$\delta(x,y) = A_{\mathrm{corr}}\sin\left(\frac{2\pi x}{\lambda}\right)\mathrm{sech}^2\left(\frac{\pi(y - y_c)}{W}\right). \tag{8}$$

Parameters relevant for the domain and bathymetry are summarized in Table 1. An illustration of the resulting bathymetry is shown in Fig. 2.

In this bathymetric setup, flow in the positive x-direction is prograde, while flow in the negative x-direction is retrograde. Prograde flow corresponds here to cyclonic circulation around a basin, with shallower water to the right of the current in this Northern Hemisphere configuration.

2.3 Forcing

The system is forced by an along-channel spatially uniform surface stress that varies sinusoidally in time. It is defined as

$$\boldsymbol{\tau}_s = \tau_{sx}\boldsymbol{i} = \tau_0 \sin\left(\frac{2\pi}{T}t\right)\boldsymbol{i}, \tag{9}$$

where T is the forcing period, and τ_0 is the maximum kinematic forcing. In the base case, we set $\tau_0 = 10^{-4}\,\mathrm{m^2\,s^{-2}}$, following values used in comparable idealized studies (e.g. Brink, 2010).

To explore the role of forcing time scales, we contrast a short and a long forcing period. For the short-period case, we use $T = 16$ days. This value lies at the longer end of what can be considered synoptic variability, but experiments with shorter

Table 1. Parameters defining the model domain and bathymetry. The domain consists of a continental slope with superimposed sinusoidal corrugations. *The baseline cases use a corrugation wavelength of 45 km, while additional runs with 22.5 km and 90 km are also considered.

Symbol	Description	Value
L_x, L_y	Domain size	90km
Δx, Δy	Grid spacing	1km
H_{sh}	Shelf depth	0.1km
H_{bs}	Basin depth	0.9km
y_c	Slope center	45km
W	Slope width	30km
A_{corr}	Corrugation amplitude	10km
λ	Corrugation wavelength	45km*

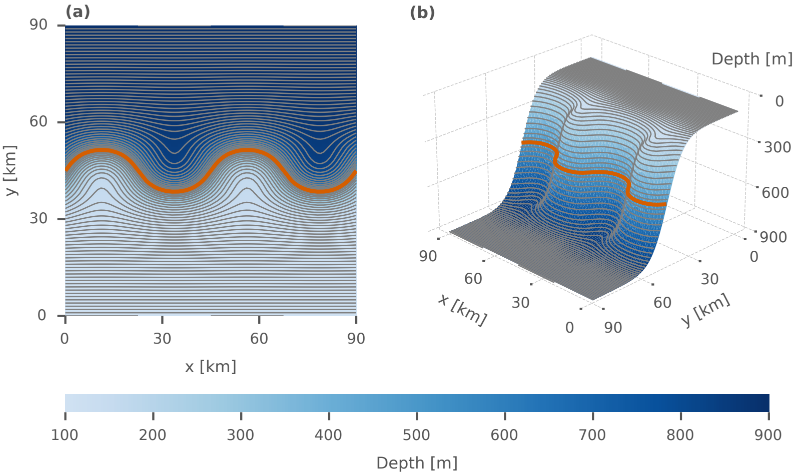

Figure 2. Model bathymetry in (a) two and (b) three dimensions. Contour lines show the constant-depth paths used in the analysis; these are not equally spaced in depth, but instead represent the mean depth associated with each y-coordinate. The mid-slope contour is highlighted.

periods in our setup exhibit qualitatively similar behavior. We therefore use 16 days as a representative fast-forcing limit, because it produces a clearer signal and facilitates interpretation of the flow response. The long-period case, with $T = 128$ days, represents slowly varying, seasonal-scale forcing. Together, these two limits bracket the essential differences between rapidly and slowly varying forcing.

The short-period experiment is run for 192 model days, while the long-period experiment is run for 384 model days. These durations are chosen to exceed the system's frictional adjustment time, and thus let the system lose memory of the initial state. After an initial transient, the model response becomes cycle-to-cycle repeatable, and we therefore analyze only the final 128 days of each simulation. The time step is 4 seconds, and output is saved every 3 model hours.

3 Integral balances

Which terms in the governing equation presented in Section 2.1 contribute to the along-slope flow? As it turns out, the answer depends on how the system is diagnosed. In this section, we examine the same system through two complementary frameworks: one following depth contours, the other cutting straight across the slope at constant y.

We define overbar notation to indicate pathwise averaging:

$$\overline{(\cdot)}^{y} \equiv \frac{1}{L_x} \oint_{0}^{L_x} (\cdot)\, dx, \quad \overline{(\cdot)}^{H} \equiv \frac{1}{L_{C(H)}} \oint_{C(H)} (\cdot)\, dl. \tag{10}$$

Here, $\overline{(\cdot)}^{y}$ denotes an average at fixed y, while $\overline{(\cdot)}^{H}$ represents an average along a closed depth contour $C(H)$, where $L_{C(H)}$ is the contour length and dl is a line segment.

In the theoretical derivations that follow, we adopt the rigid-lid approximation and thus neglect the contribution of the free-surface displacement η to the total layer thickness $D = H + \eta$, so that $D \approx H$. This approximation is appropriate here because the barotropic Rossby radius of deformation is much larger than the horizontal scales of the flow considered (Gill, 1982).

3.1 Momentum budget integrated along depth contours

Along closed depth contours, the momentum balance takes on a particularly simple form. Integrating the momentum equation given by Eq. (5) along a closed depth contour $C(H)$ yields the contour-integrated momentum balance

$$H\partial_t \overline{\boldsymbol{u}\cdot\boldsymbol{t}}^{H} = H\overline{\zeta\boldsymbol{u}\cdot\boldsymbol{n}}^{H} + \overline{\boldsymbol{\tau}_s\cdot\boldsymbol{t}}^{H} - R\overline{\boldsymbol{u}\cdot\boldsymbol{t}}^{H}, \tag{11}$$

where $\boldsymbol{t}$ and $\boldsymbol{n}$ are the tangent and normal unit vectors to the contour, respectively. The normal unit vector $\boldsymbol{n}$ is defined to point in the direction of increasing depth.

In obtaining Eq. (11), we use that the projection $(\boldsymbol{k}\times\boldsymbol{u})\cdot\boldsymbol{t}$ introduces the cross-contour velocity, producing the depth-integrated flux $H\zeta\,\boldsymbol{u}\cdot\boldsymbol{n}$. The associated planetary vorticity term $Hf\,\boldsymbol{u}\cdot\boldsymbol{n}$ is proportional to the cross-contour volume flux under the f-plane approximation, and therefore vanishes under the rigid-lid assumption when integrated around the re-entrant domain. The pressure and kinetic-energy gradients do not contribute, since H can be factored out and the remaining gradient term integrates to zero along any closed contour.

The first term on the right-hand side of Eq. (11) represents the depth-integrated flux of relative vorticity across the contour in the offshore direction. The second term reflects the tangential projection of the surface stress, and the final term represents damping by linear bottom drag.

The linear version of Eq (11) is an ordinary differential equation, and can be solved to obtain an analytical model for the circulation around depth contours. Neglecting the nonlinear term and using the integrating factor $\exp(Rt/H)$, we get

$$\overline{\boldsymbol{u}\cdot\boldsymbol{t}}^{H} = \exp\left(-\frac{R}{H}t\right)\overline{\boldsymbol{u}_0\cdot\boldsymbol{t}}^{H} + \int_{0}^{t} \exp\left[-\frac{R}{H}(t-t')\right]\frac{F}{H}\,dt', \tag{12}$$

where

$$F = \overline{\boldsymbol{\tau}_s \cdot \boldsymbol{t}}^H \tag{13}$$

is the forcing by surface stress. The first term on the right-hand side of Eq. (12) is the exponentially decaying contribution from the initial state $\overline{\boldsymbol{u}_0 \cdot \boldsymbol{t}}^H$, while the second term is a convolution between the forcing term F and an exponential kernel. In other words, Eq. (12) shows that the linear ocean response is a lagged and smoothed version of the forcing. Given our typical value for R, the factor H/R corresponds to frictional spin-down times of 2–21 days across the domain depths $100-900\,\mathrm{m}$, indicating how quickly the system adjusts to forcing.

Equation (12) corresponds to the simplified linear model of time variable flow along f/H-contours of Isachsen et al. (2003), but with the additional approximation of a constant f. The same diagnostic was later used by Sjur et al. (2025) and Johnston et al. (2025) to estimate wind-driven circulation in realistic Arctic simulations and in observations. The latter study also diagnosed the nonlinear vorticity flux term in high-resolution simulations and included it as a forcing term, so that

$$F = \overline{\boldsymbol{\tau}_s \cdot \boldsymbol{t}}^H + H\overline{\zeta \boldsymbol{u} \cdot \boldsymbol{n}}^H. \tag{14}$$

In this study, Eqs. (12) and (13) will serve as a linear reference for evaluating the response.

We can further utilize the linear version of Eq. (11) to estimate the maximum velocity of the response to the surface stress given by Eq. (9). Because the stress is purely zonal and uniform, its contour-mean projection is reduced by the geometric factor $L_x/L_{C(H)}$. Solving Eq. (11) for a periodic forcing of frequency $\omega = 2\pi/T$ gives the maximum along-contour velocity amplitude

$$u_{\max}(H) = \frac{L_x}{L_{C(H)}} \frac{\tau_0}{R} \left[1 + \left(\frac{\omega H}{R}\right)^2\right]^{-1/2}, \tag{15}$$

with derivation provided in Appendix B1.

From Eq. (15), we see that for $\omega \ll R/H$ (long forcing periods), the flow amplitude is dependent on depth only through the geometric factor, approaching $\left(L_x/L_{C(H)}\right)(\tau_0/R)$. In contrast, rapidly oscillating forcing with $\omega \gg R/H$ is expected to produce a weaker response with a stronger depth dependence.

3.2 Momentum budget integrated along constant y transects

The same system is described by a different momentum balance when integrated along straight transects. Integrating Eq. (1) along the channel at fixed y, we obtain a budget for the depth-integrated x-momentum,

$$\partial_t \overline{Hu}^y = -\overline{\partial_y (Huv)}^y - \overline{H\,\partial_x \phi}^y + \overline{\tau_{sx}}^y - R\overline{u}^y. \tag{16}$$

The first term on the right-hand side represents the convergence of depth-integrated momentum flux. The second term, involving the correlation between the dynamic pressure and bottom slope, corresponds to topographic form stress, that is the pressure work done against the corrugated bottom. Importantly, nonzero form stress requires a phase offset between pressure and the underlying bottom corrugations. Without such an offset, the integral vanishes. The third term represents direct wind forcing in the x direction, and the final term accounts for linear bottom drag opposing the flow. As for the analysis along constant depth contours, the term associated with planetary vorticity becomes proportional to the cross-contour volume flux, and thus integrates to zero under the rigid-lid approximation.

3.3 Potential vorticity perspective

At first glance, the two momentum budgets emphasize different mechanisms in addition to surface and bottom stresses: vorticity fluxes when the balance is evaluated along depth contours, and form stress together with momentum flux convergence when evaluated along straight transects. As it turns out, however, these terms can be interpreted to reflect the same mechanism. Specifically, under quasi-geostrophic assumptions, both frameworks can be interpreted to describe a flux of potential vorticity (PV) across the slope.

For reference, the quasi-geostrophic potential vorticity (QGPV) of a one-layer shallow-water system over weak topography is given by

$$q = \zeta + \frac{fh}{H_0}, \tag{17}$$

where the total depth has been decomposed as $H(x,y) = H_0(y) - h(x,y)$. Here, H_0 denotes the mean depth along constant-y contours and h represents deviations associated with topographic corrugations, assumed to be small compared to H_0.

We now show how this QGPV emerges naturally in the fixed-y momentum budget. Consider the first two terms on the right-hand side of Eq. (16), namely the convergence of depth-integrated momentum flux and the topographic form stress. We define their sum as $\overline{Q}^y$, and use the identity in Eq. (3) to re-write it as

$$\overline{Q}^y = \overline{H\zeta v}^y - \overline{H\partial_x\left(\phi + \tfrac{1}{2}\boldsymbol{u}\cdot\boldsymbol{u}\right)}^y. \tag{18}$$

For small Rossby numbers, geostrophic scaling implies that the pressure term dominates the kinetic-energy contribution, $|\phi| \gg \frac{1}{2}|\boldsymbol{u}|^2$, allowing the latter to be neglected. Substituting the depth decomposition into Eq. (18) then yields

$$\overline{Q}^y = H_0\,\overline{\zeta v}^y - \overline{h\,\partial_x\phi}^y + \overline{h\,\zeta v}^y. \tag{19}$$

Since the topographic variations are assumed to be small compared to the background depth, the final term can be neglected. Finally, using geostrophic balance, $\partial_x\phi = f v_g$, we obtain

$$\overline{Q}^y \approx H_0\left(\overline{\zeta v}^y + \overline{\frac{f v_g h}{H_0}}^y\right). \tag{20}$$

The bracketed term in Eq. (20) has the form of a QGPV flux across constant-y contours. In particular, under quasi-geostrophic scaling, the advecting velocity may be taken as geostrophic to leading order, such that the combination of terms can be written as

$$\overline{Q}^y \approx \overline{q v_g}^y, \tag{21}$$

with q defined in Eq. (17). Thus, under quasi-geostrophic assumptions, the combined effect of nonlinear advection and topographic form stress in the fixed-y momentum balance can be interpreted as a flux of potential vorticity across constant-y contours.

In the depth-following formulation, the situation simplifies further. Along contours of constant depth, the topographic contribution fh/H_0 to the QGPV is constant by construction, and the corresponding flux is therefore proportional to the cross-contour volume transport. The topographic contribution to the flux is thus zero under the rigid-lid assumption, and the QGPV flux reduces to a flux of relative vorticity alone. This is precisely the nonlinear term appearing in the contour-integrated momentum balance (Eq. 11). Interpreting the dynamics in terms of PV fluxes thus provides a unifying framework, showing that the fixed-y and depth-contour diagnostics can be understood as reflecting the same underlying PV flux. We can hence write the momentum balance in a general form as

$$H_0 \partial_t \overline{\boldsymbol{u} \cdot \boldsymbol{t}} = H_0 \overline{q \boldsymbol{u} \cdot \boldsymbol{n}} + \overline{\boldsymbol{\tau}_s \cdot \boldsymbol{t}} - R \overline{\boldsymbol{u} \cdot \boldsymbol{t}}, \tag{22}$$

where the overbar denotes an average either along fixed-y or constant depth contours. Further, although topographic effects do not appear explicitly in the depth-following formulation, their influence on the flow is included implicitly in the relative vorticity flux through the conservation of q.

We emphasize that this PV-based interpretation relies on quasi-geostrophic assumptions, including small Rossby number and weak topographic slopes. While not exact, it provides a useful conceptual framework for relating the two diagnostic approaches.

3.4 Domain-integrated transport

We will extend our theoretical analysis to examine the total transport through the domain. To do so, we integrate Eq. (16) in the y-direction, yielding:

$$\partial_t \langle Hu \rangle = -\langle H \partial_x \phi \rangle + \langle \tau_{sx} \rangle - R \langle u \rangle, \tag{23}$$

where

$$\langle (\cdot) \rangle \equiv \frac{1}{A} \iint (\cdot)\, dx\, dy \tag{24}$$

denotes the area average over the domain. Here, A is the total area. This equation expresses the time evolution of the domain-averaged transport as dependent on three terms: the domain-averaged topographic form stress, the domain-averaged surface stress, and the domain-averaged bottom drag, all in the x-direction. We have here utilized the no-flux condition at the y-boundaries. Notably, the nonlinear momentum flux convergence in Eq. (16) then integrates to zero, reflecting that nonlinear advection only redistributes momentum within the domain.

Let's now consider the evolution of the total transport over a forcing period T, following Brink (2010). If the surface stress integrates to zero over T, and there is no slow drift so that $\partial_t \langle Hu \rangle$ also integrates to zero, then the residual balance is solely between bottom drag, proportional to a residual flow, and topographic form stress. In other words, form stress is the mechanism that can sustain a residual transport.

Given its central role in the domain-integrated budget, the apparent absence of topographic form stress in the depth-following framework demands further comment. To address this, we return to the pressure term in Eq. (1) and evaluate it along depth-following contours $C(H)$, but this time integrating over the full domain. To do so, we need to express an area element in depth-following coordinates. We utilize that neighboring contours separated by a depth increment dH are spaced a normal distance $dn = dH/|\nabla H|$ apart. The area element in the depth-following coordinates is thus given by

$$dA = dl\,dn = dl\,\frac{dH}{|\nabla H|}, \tag{25}$$

where dl is a line segment along a depth contour. Integrating first along the contours and then over the full depth range yields

$$\iint\limits_{A} H\boldsymbol{\nabla}\phi\cdot\boldsymbol{t}\,dA = \int\limits_{H_{y=0}}^{H_{y=L_y}} H\left[\oint\limits_{C(H)} |\nabla H|^{-1}\boldsymbol{\nabla}\phi\cdot\boldsymbol{t}\,dl\right] dH. \tag{26}$$

In the last expression, the pressure contribution is weighted by the local inverse slope $|\nabla H|^{-1}$, and the inner contour integral does not generally vanish. Thus, while topographic form stress cancels when integrated along a single depth contour, it still enters the domain-integrated balance. In practice, however, evaluating this expression is numerically challenging, as the integration along depth contours does not align with the discrete model grid, and great care must be taken to precisely cover the full domain.

4 Simulation results

4.1 Comparing mid-slope circulation with linear estimates

Do the nonlinear deviations identified in realistic Arctic Ocean simulations also emerge in a stripped-down, idealized setting? To address this question, we apply the same diagnostic used for the realistic simulation in Fig. 1 to the idealized model experiments. Specifically, we examine scatterplots of the simulated mid-slope circulation against linear estimates given by Eqs. (12) and (13), for both long and short forcing periods (Fig. 3). The circulation is diagnosed along the mid-slope depth contour (highlighted in Fig. 2), allowing direct comparison with linear theory. Perfect agreement with the linear estimates would place points along the 1:1 line.

From Fig. 3, we see that both deviations from linear theory can be reproduced, though their expression depends on forcing period. In particular, the long forcing period (Fig. 3a) yields a clear prograde–retrograde asymmetry, with a clear bend in the scatter, while the short forcing period (Fig. 3b) shows only a sustained prograde shift. Thus, we see indication of the nonlinear contribution being dependent on forcing period. Note, however, that maximum circulation strength also differs considerably between the two experiments, a point we will return to later. Notably, both forcing periods show signs of hysteresis. The hysteresis is most pronounced in the long forcing case, with data separated into two distinct branches, one near linear theory and one displaced in the prograde direction.

https://doi.org/10.5194/egusphere-2026-778
Preprint. Discussion started: 17 February 2026

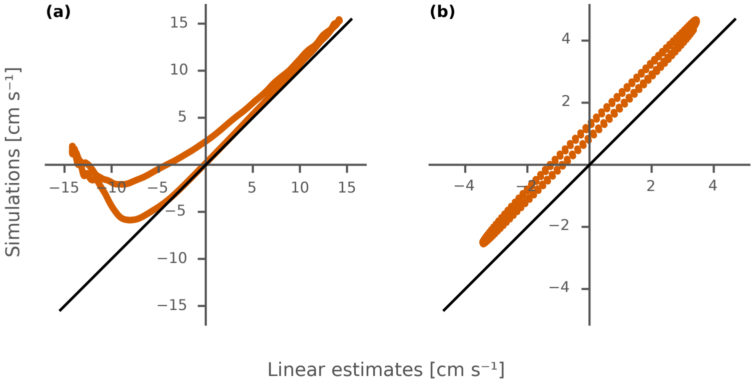

Figure 3. Scatterplots comparing circulation (normalized with contour length) along a depth contour with linear estimates. The relevant contour is highlighted in Fig. 2. Results for a forcing period of (a) 128 days, and (b) 16 days, are shown. Black lines indicate the 1:1 reference.

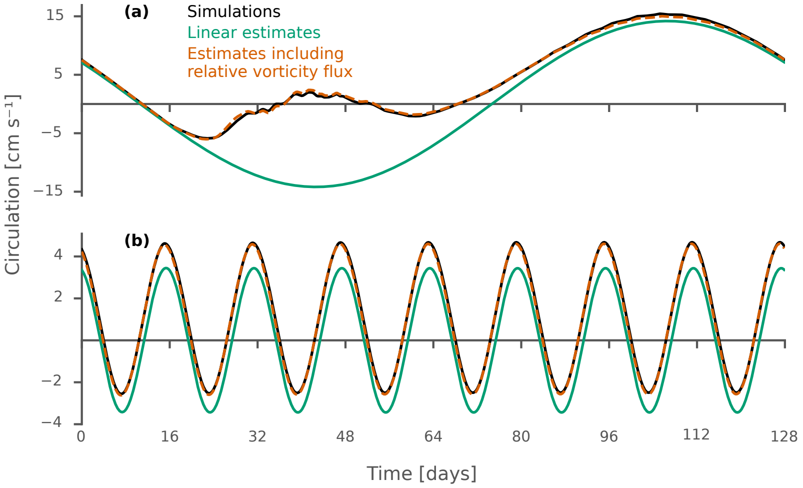

Figure 4. Time series of circulation (normalized with contour length) along a depth contour for a forcing period of (a) 128 days, and (b) 16 days. Estimates including the nonlinear relative vorticity flux contribution are drawn in dashed lines, and fall on top of the circulation diagnosed from simulations. The relevant contour is highlighted in Fig. 2.

To investigate when in the forcing cycle nonlinear deviations emerge, we turn to time-series of circulation, shown in Fig. 4. We set $t = 0$ to be at the beginning of a retrograde forcing period. Throughout, we refer to intervals during which the linear esti-

https://doi.org/10.5194/egusphere-2026-778
Preprint. Discussion started: 17 February 2026

mate predicts negative circulation as the retrograde phase, and to intervals with predicted positive values as the prograde phase. For the long forcing period (Fig. 4a), the circulation initially follows the linear prediction as the system enters the prograde phase. Deviation from linear theory then sets in, first gradually, then it abruptly becomes more pronounced (approximately 25 days into retrograde forcing), leading to a strong departure. At this point, the system enters a regime where retrograde circulation no longer strengthens, despite increasing forcing. We will refer to this behaviour as *saturation*. As the system moves into the prograde phase, the circulation gradually converges back toward the linear estimate. This shows that the lower branch of the corresponding scatterplot (Fig. 3a) stems from the prograde to retrograde transition, while the upper branch corresponds to the retrograde to prograde transition.

For the short forcing period (Fig. 4b), the circulation remains closer to the linear estimate throughout the forcing cycle, consistent with the lack of bending seen in the scatterplots. As noted, the main feature here is a sustained prograde shift. However, there are slightly larger offsets during transitions from the retrograde to the prograde phase than in the opposite direction. In other words, the system is without signs of saturation, but with an increased offset at the end of the retrograde phase, giving rise to the hysteresis seen in the scatterplot.

The nonlinear contribution relevant for depth-following circulation is a flux of relative vorticity across the depth-contour (Eq. 11). In Fig. 4, the dashed lines show estimates where diagnosed relative vorticity fluxes have been included as a forcing term (using Eq. 14 as forcing term in Eq. 12). For both forcing periods, including relative vorticity fluxes in the estimates almost entirely removes the discrepancy with the simulations. This agreement indicates that the observed nonlinear deviations from linear theory can indeed be understood as the consequence of a single nonlinear mechanism, namely a cross-contour fluxes of relative vorticity.

4.2 Spatial and temporal dependence

Depth-contour analysis

So far, we have focused on circulation along the mid-slope depth contour. The view is now broadened to the entire domain, examining how the circulation and the various terms in the integrated momentum equation vary over one forcing cycle and across the slope (Fig. 5). As a reminder, for circulation along depth contours, the contributing terms are the surface stress, bottom stress, and the nonlinear relative vorticity flux term.

Panel (a) and (b) in Fig. 5, one for each forcing period, contain three components: (i) time evolution of momentum terms for the mid-slope contour, (ii) a Hovmöller diagram of circulation, with time on the horizontal axis, depth on the vertical axis, and (iii) cycle-mean profiles of momentum terms as a function of contour depth. While the top sub-panels (i) show time-series for the mid-slope depth contour only, the patterns are broadly representative of other depths as well (see Fig. A1 for full Hovmöller diagrams of the individual terms). An imbalance between the momentum term signify acceleration.

For both forcing periods, the depth and time-dependent structure of the circulation broadly follows the behavior predicted by linear theory (Eq. 12). In particular, the circulation lags the surface stress by an amount that increases toward deeper contours, as expected from the linear response. This lag is evident, for example, in the delayed transition from prograde to retrograde

https://doi.org/10.5194/egusphere-2026-778
Preprint. Discussion started: 17 February 2026

circulation at greater depths. The depth dependence of the response amplitude is more pronounced for the short forcing period (Fig. 5bii), consistent with Eq. (15).

Superimposed on this largely linear response, clear signs of saturation emerge for the long forcing period (Fig. 5a). During the retrograde phase, the amplitude of retrograde circulation ceases to increase, first near 364 m depth, after which the saturated region gradually expands offshore. In contrast, no such saturation occurs anywhere along the slope for the short forcing period (Fig. 5b).

The momentum diagnostics clarify the origins of the deviations from linear theory. For both long and short forcing periods, cycle-mean diagnostics (Fig. 5aiii and Fig. 5biii) show that vorticity fluxes provide a net prograde tendency across the slope, strongest at mid-slope depths. The flux is directed down the background potential vorticity gradient, from shallow toward deeper water, and is balanced by bottom friction, implying a residual prograde circulation over a forcing cycle. Compared with the long-period case, the cycle-mean flux maximum for short forcing is shifted onshore, consistent with the stronger depth dependence of the circulation response.

For the long forcing period, relative vorticity fluxes increase sharply at the onset of saturation and remain elevated throughout the retrograde phase (Fig. 5ai), capping the circulation strength. An exception from this pattern is found offshore of the slope, where relative vorticity fluxes temporarily take on retrograde values during the retrograde phase (Fig. A1). Animations of the flow show that the abrupt rise in fluxes coincides with the emergence of transient eddies, consistent with vorticity being exported across depth contours (see supplementary video). We note that Constantinou and Young (2017) have discussed a somewhat analogous saturation phenomenon, where the emergence of transient eddies strongly reduces the mean-flow response to retrograde wind forcing. Because of inertia, the system retains a memory of this elevated prograde state even after the fluxes subside, generating the hysteresis observed in the scatterplots. This behavior follows directly from Eq. (12), which links circulation to the time-integrated forcing, and thus predicts the circulation to inherently carry a memory of past states over a time-scale H/R. During strong prograde forcing, relative vorticity fluxes oscillate, producing a weak prograde tendency in that phase as well.

For the short forcing period, vorticity fluxes are weaker and alternate in sign through the cycle, but still average to a net prograde tendency, with the highest prograde values during the retrograde phase. Exactly when this maximum occurs during the retrograde phase depends on depth (Fig. A1). The system's memory smooths these fluctuations, leaving a residual prograde offset visible in both scatterplots and time series.

Constant-y analysis

Having established how relative vorticity fluxes contribute to the circulation along depth contours, we now complement this with an analysis following constant-y contours (Fig. 6). In this framework, the nonlinear contribution is the full momentum flux convergence, and topographic form stress appears explicitly. The simpler geometry also allows for area integrals: the top panels now show area-integrated momentum balances as functions of time, while crosses above the bottom-right panels indicate time- and area-mean values over the domain and one forcing cycle. Individual Hovmöller diagrams for each momentum term can be found in Fig. A2.

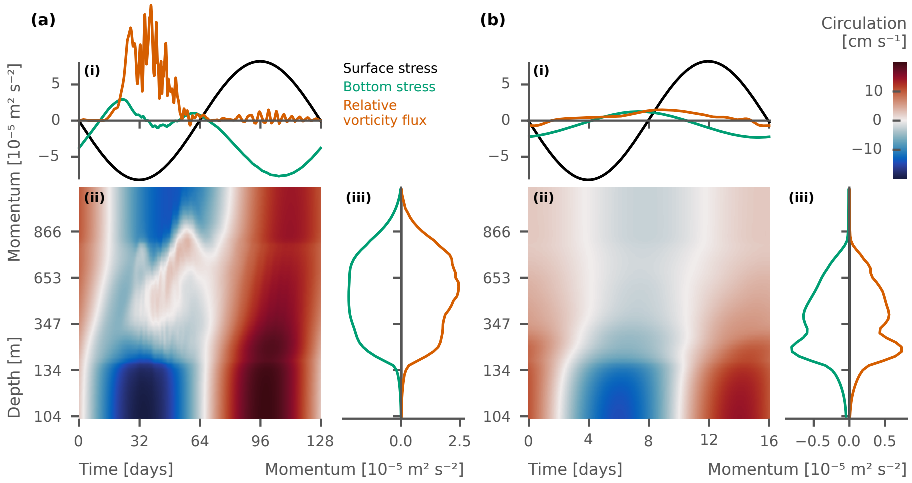

Figure 5. Momentum terms along depth contours. Results for a forcing period of (a) 128 days, and (b) 16 days are shown. Each sub-figure contains three diagnostics: (i) momentum terms for the mid-slope depth contour as a function of time; (ii) a Hovmöller diagram of depth-integrated circulation (time on the horizontal axis, depth on the vertical axis); and (iii) time-mean momentum terms over one forcing cycle as a function of depth. The momentum terms are defined in Eq. (11). Note that the depth contours are equally spaced in y (not depth), and correspond to the y-values in Fig. 6. Depth contours are shown in Fig. 2.

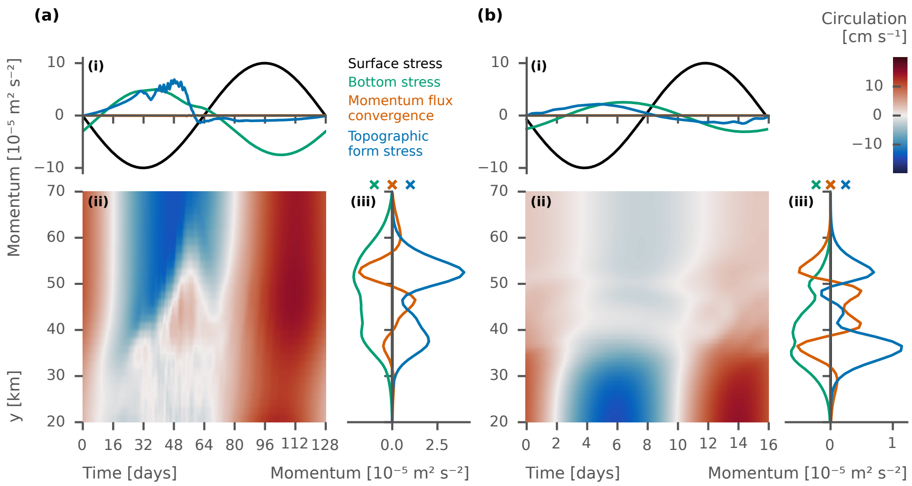

Figure 6. Momentum terms along constant-y contours. Results for a forcing period of (a) 128 days, and (b) 16 days are shown. Each sub-figure contains the following diagnostics: (i) area-mean momentum terms as a function of time; (ii) a Hovmöller diagram of depth-integrated circulation (time on the horizontal axis, y on the vertical axis); and (iii) time-mean momentum terms over one forcing cycle, with crosses above the panels indicating the area and time-mean balance. The momentum terms are defined in Eq. (16).

We first note that the circulation is qualitatively similar to that along depth-contours; both forcing periods show a phase lag between surface stress and circulation that increases with depth. There is also a stronger depth dependence for the short forcing period, and saturation during the retrograde phase for the long forcing period.

A key result here is that momentum flux convergence integrates to zero across the slope for both forcing periods (Fig. 6ai and Fig. 6bi). This is a reminder that it acts only to redistribute momentum along the slope, without contributing to the domain-integrated balance. The time and area-mean balance is instead between topographic form stress and bottom stress (crosses above Fig. 6aii and Fig. 6bii), consistent with theory described in Sec. 3.4. This point is crucial, because it shows that although form stress does not appear in the depth-following framework, it is central for the residual transport integrated across the channel.

The time evolution of the area-integrated balances (top panels of Fig. 6) highlights the role of topographic form stress in shaping the time-dependent circulation. For the long forcing period, topographic form stress is strongly prograde during the retrograde phase, with high values coinciding with saturation of the circulation, and weakly retrograde during the prograde phase. This phase-dependent asymmetry mirrors findings from steady-state analyses, where retrograde flow generates stronger topographic form stress (e.g., Bai et al., 2021). For the short forcing period, form stress alternates in sign within each cycle, but averages to a slight prograde bias, consistent with a residual prograde tendency.

Across the slope, momentum flux redistributes momentum (Fig. 6aiii and Fig. 6biii). For the long forcing period, the time-mean momentum flux convergence is prograde at mid-slope (driving prograde flow) and retrograde on either side (driving retrograde flow), with an additional convergence region offshore. The time-variable momentum flux convergence shows a similar pattern mainly during the retrograde phase (Fig. A2), indicating that the time-mean structure captures a persistent, phase-dependent aspect of the flow. The time-mean form stress is prograde for all y, but peaks on the flanks where retrograde momentum flux convergence occurs. These peaks likely mark regions of topographic Rossby-wave generation, which in turn drive retrograde momentum-flux convergence, whereas over the mid-slope, wave breaking and eddy potential vorticity mixing promote prograde convergence (see, e.g., Dritschel and McIntyre, 2008). For the short forcing period, the overall pattern is similar, but a pronounced dip in momentum flux convergence appears over the mid-slope, coinciding with an increase in topographic form stress.

4.3 Unified analysis in terms of PV fluxes

As shown in Sec. 3.3, both the depth-following and constant-y framework can be interpreted in light of fluxes of quasi-geostrophic potential vorticity (QGPV) across the slope. We now test this interpretation by diagnosing the cross-slope QGPV flux in both frameworks and comparing their spatial structure and magnitude. Figure 7 shows the time-mean QGPV flux and the bottom stress, which according to theory balances the flux, for the long (a) and short (b) forcing periods. Results from the depth-following and constant-y frameworks are shown together for direct comparison. As described in Sec. 3.3, in the depth-following framework, the QGPV flux is entirely accomplished by the relative vorticity flux. In the constant-y framework, the QGPV flux can be approximated by combining the momentum flux convergence and the topographic form stress. These two contributions tend to be anti-correlated (see Fig. 6). Their sum, however, constitutes a net flux of QGPV across the slope, which is the quantity shown in Fig. 7. We verified this interpretation by also computing the cross-contour flux of QGPV (as defined in Eq. 17) directly. This direct calculation yields qualitatively similar spatial patterns and magnitudes, with discrepancies confined primarily to the steepest part of the slope.

https://doi.org/10.5194/egusphere-2026-778
Preprint. Discussion started: 17 February 2026

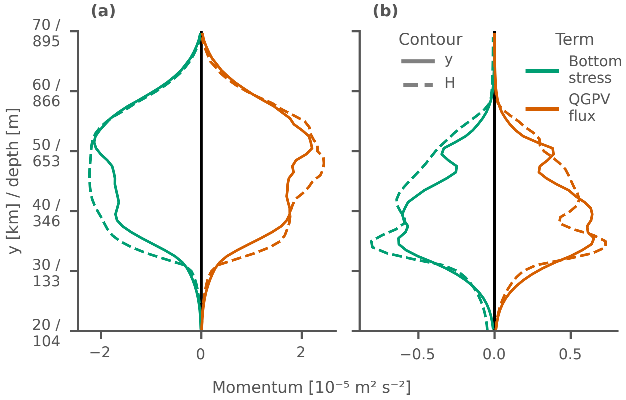

Figure 7. Time-mean quasi-geostrophic potential vorticity (QGPV) flux and bottom stress diagnosed from the depth-following and constant-y frameworks. Results are shown for (a) a forcing period of 128 days and (b) a forcing period of 16 days. Positive QGPV flux indicates offshore transport, down the large-scale PV gradient.

In both forcing regimes, and for both integration paths, the time-mean QGPV flux is directed offshore, down the large-scale PV gradient, and approximately balances the vorticity removal by bottom stress associated with the time-mean residual flow along the slope. The cross-slope structure of the diagnosed QGPV flux shows a strong structural agreement between the depth-following and constant-y frameworks, with comparable magnitudes and spatial organization across the slope. Small differences remain, which are likely related to geometric factors: a depth-following contour is generally curved and longer than a straight y-transect, leading to differences in bottom stresses and associated balancing QGPV fluxes. Nevertheless, the two diagnostics consistently identify a systematic offshore QGPV flux that maintains the residual prograde slope circulation.

4.4 Comparison with arrested wave theory

In earlier sections, we found that saturation strongly influences the retrograde response to long forcing periods, whereas it is absent for short-period forcing. In this section, we focus on the response to the long forcing period and investigate the mechanism responsible for the observed saturation.

Leaning on earlier steady-state studies (Bai et al., 2021; Zhang and Lentz, 2017), we hypothesize that saturation occurs when topographic Rossby waves with wavelengths comparable to the bathymetric corrugations are arrested by the mean flow. In this case, the saturated flow speed is expected to scale with the intrinsic phase speed of these waves. Because the phase speed depends on wavelength, this mechanism predicts different saturation levels for different corrugation scales.

To test this idea, we compute arrest speeds using the linear barotropic coastal-wave model of Brink (2025). For a range of wavelengths, we calculate the phase speeds of the first three topographic Rossby wave modes and compare these with the saturation velocities diagnosed from the simulations. The model configuration used for the calculations is provided in the supplementary material. We note that some caveats apply; the wave model assumes steady, linear dynamics and is here applied

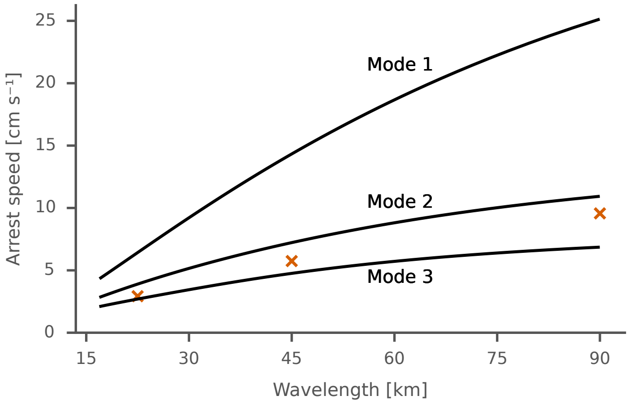

Figure 8. Theoretical arrest speed for topographic Rossby waves as a function of wavelength, and diagnosed saturation speed. Solid lines show theoretical arrest speeds for mode 1 (top), mode 2 (middle), and mode 3 (bottom), where the mode number signify the number of zero crossings in the pressure modal function. Crosses indicate the saturation speed from simulations with topographic wavelengths $\lambda = 22.5$, 45, and 90 km. Simulations were run with a forcing period of 128 days.

without any imposed mean along-slope velocity, whereas our simulations involve time-dependent forcing. Nevertheless, for the slowly varying cases of interest, these linear estimates provide a useful approximation to the arrest speeds.

Saturation speeds are estimated as the maximum retrograde circulation along depth contours spanning the central slope (contour indices 40–50, corresponding to depths of roughly 360–670 m), providing an upper-bound estimate. To test whether the saturation speed follows the expected wavelength dependence, we conducted experiments with corrugation wavelengths λ of 22.5, 45, and 90 km. The theoretical arrest speeds and the diagnosed saturation speeds are shown in Fig. 8. As we see, the diagnosed saturation speeds exhibit a similar wavelength dependence as expected for the arrest of topographic Rossby waves, with increasing speed as the wavelength increases. The arrest speeds fall between mode 2 and 3, but seem to follow mode 2 better as the wavelength increases.

To further test whether the observed saturation reflects the arrest of topographic Rossby waves, we analyze the cross-slope structure of the simulated pressure field at the onset of saturation ($t = 30$ days). The goal is to determine whether the simulated pattern resembles the mode structure expected for an arrested topographic Rossby wave. To isolate a possible mode structure, we compute residual pressure perturbations ϕ' from the model output. Obtaining a suitable ϕ' is not straightforward, since the corrugated bathymetry imprints a strong, cycle-dependent pattern on the pressure field. This imprint is not stationary, but alternates in sign between the prograde and retrograde phases, reflecting the reversal of along-slope flow. To suppress this bathymetric imprint while retaining any coherent trapped-wave structure, we combine the retrograde state, potentially containing a trapped mode, with the prograde state (shifted by half a period relative to the retrograde state), so that the two are in exact antiphase. Adding these anti-phase fields cancels the alternating topographic imprint and leaves any phase-dependent signal. We note that a small contribution from the residual flow may remain. Additionally, the cross-slope mean is removed from each snapshot of ϕ to eliminate the large-scale along-slope tilt.

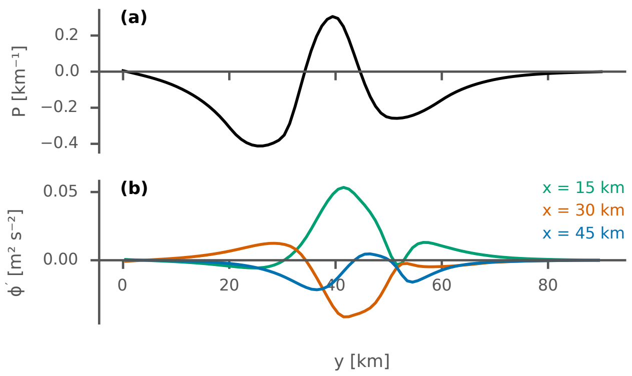

Figure 9. Panel (a) shows the theoretical cross-slope mode 2 structure for a wavelength of 45 km. Panel (b) shows the residual dynamic pressure from simulations for a wavelength of 45 km at different x-positions, used as a proxy for the mode structure. The procedure for estimating this diagnostic is described in the main text. Simulations were run with a forcing period of 128 days.

Figure 9 compares the residual pressure ϕ' with the theoretical cross-slope pressure structure of a 45 km mode 2 topographic Rossby wave, computed using the wave model of Brink (2025). The simulation ϕ' reveals a pattern similar to that of a mode 2 wave, with alternating maxima and minima across the slope that resemble the theoretical structure. Further, we see different phases of the same wave pattern for different x-positions. The match is not exact, with curves slightly displaced in the vertical (likely reflecting contamination by the residual flow), but the extrema align well with theory. Albeit not perfect, this structural match supports the interpretation that the observed saturation arises from the arrest of topographic Rossby waves.

We note that the arrest of a mode 2 wave is consistent with the findings of Zhang and Lentz (2017), who analyzed wind-driven retrograde flow over a shelf valley in terms of coastal-trapped wave characteristics. In their study, the bathymetry consisted of a single valley, allowing the cross-slope structure of the resulting lee waves to be compared more directly with theoretical mode structure.

4.5 Varying the forcing strength

We now turn to investigate why saturation is absent in the simulations with rapidly oscillating forcing. Building on the long-period results, where saturation can be linked to the arrest of topographic Rossby waves, we hypothesize that the shorter-period forcing simply does not generate flow strong enough to arrest such waves. To test this, we perform an additional set of simulations in which the surface forcing amplitude is systematically increased, so that the short-period runs reach the theoretical arrest speeds.

The results are summarized in Fig. 10. Panel (a) shows the maximum prograde circulation along three different depth contours at the mid-slope and its flanks. These velocities scale linearly with forcing strength, consistent with the theoretical linear prediction from Eq. (15). The slope of this relationship increases toward shallower depths and for longer forcing periods, with the depth dependence especially pronounced for the short-period case, as expected from linear theory.

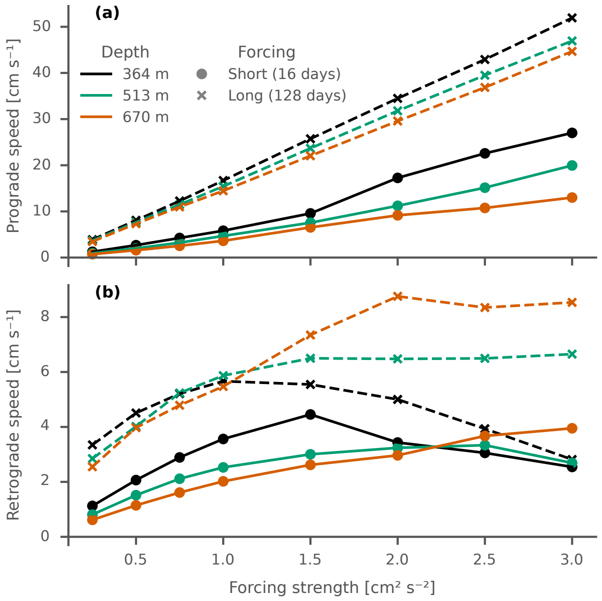

Figure 10. Maximum prograde and retrograde circulation as function of forcing strength. Panel (a) shows maximum prograde velocity along selected depth contours along the mid-slope and its flanks, and panel (b) shows maximum retrograde velocity along the same contours. Solid lines denote the 16 day forcing period and dashed lines the 128 day period.

Figure 10b shows the maximum retrograde circulation as a function of forcing strength, where the signature of saturation becomes evident. At weak forcing, retrograde speeds increase nearly linearly, but at higher amplitudes the response levels off, with the limiting speed varying by depth. At shallow contours, the speed begins to decline as the forcing further strengthens, whereas at deeper contours it continues to increase before eventually plateauing. This offshore progression indicates that the strongest retrograde flow shifts towards deeper water as the forcing intensifies. Both forcing periods display this behavior, but saturation occurs at lower speeds for the short-period case. The difference in maximum retrograde speed likely reflects that the short-period runs does not reach a steady arrested state, whereas the long-period runs approach steady conditions. Nonetheless, the analysis demonstrates that retrograde flow in the short-period simulations also saturates when the forcing is sufficiently strong, accompanied by an offshore shift in the flow maximum.

4.6 The need for corrugations

So far, all simulations considered in this study have included topographic corrugations. A direct theoretical implication of the absence of such along-slope depth variations, and thus of topographic form stress, is that oscillatory wind forcing with zero time mean cannot produce a domain-mean residual flow, as indicated by the domain-integrated momentum balance (Eq. 23). To illustrate this theoretical constraint explicitly, we now examine a set of simulations in which the slope is smooth. These

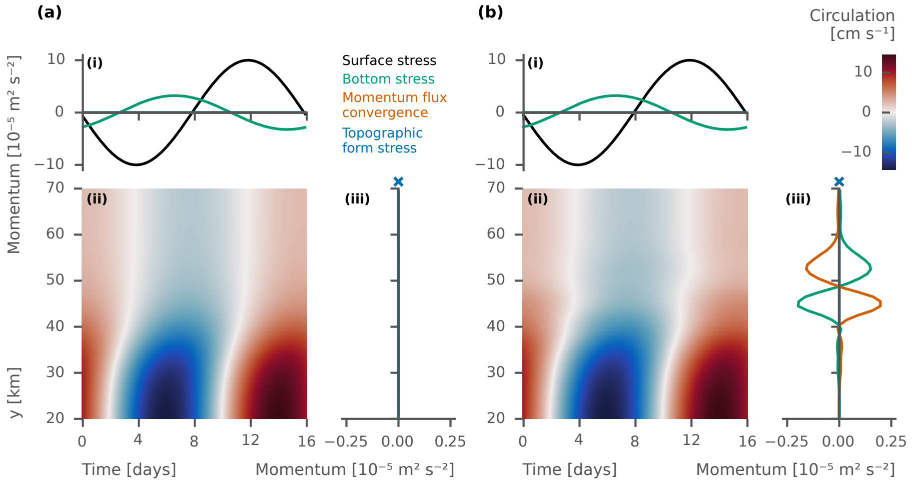

Figure 11. Momentum terms along straight depth contours for a bathymetry without corrugations. Results are shown for (a) purely along-slope wind forcing and (b) wind forcing with an imposed cross-slope component. The forcing period is 16 days in both cases. Note that relative vorticity fluxes and momentum flux convergence are identical when evaluated along straight transects without corrugations.

simulations share the same large-scale geometry and mean slope as the corrugated cases, but lack depth variations along constant-y contours. In this configuration, analyses along constant-y and along depth-following contours coincide.

We first examine the response to the standard along-slope wind forcing (Eq. 9), shown in Fig. 11a. In this case, the surface stress is spatially uniform and purely along-slope. We find that the response is well described by linear theory: the flow oscillates in time according to linear analytical estimates (Eq. 12) and produces no residual mean flow at any point along the slope. This is illustrated by the zero time mean of all momentum terms in panel (iii).

The purely linear response may reflect the fact that the applied stress is everywhere parallel to the slope and does not induce any cross-slope motion. In the presence of topographic corrugations, however, the same along-slope forcing is observed to generates cross-slope flow. To probe whether cross-slope motion alone alter the system's response, we therefore perform an additional experiment in which a cross-slope flow component is forced explicitly by the wind, while keeping the topography smooth.

This modified surface stress, denoted $\boldsymbol{\tau}_s^{cs}$, is constructed to be tangential to the bathymetric contours of the *corrugated* slope configuration used in the other experiments, while retaining the standard along-slope stress amplitude. It takes the form

$$\boldsymbol{\tau}_s^{cs} = \tau_{sx}\,\boldsymbol{i} + \tau_{sx}\,\frac{\partial_x H}{\partial_y H}\,\boldsymbol{j}, \tag{27}$$

with H and τ_{sx} as defined in Eqs. (7) and (9). The curl of this wind stress varies on horizontal scales comparable to those of the bathymetric corrugations in the corrugated-slope experiments, representing an Ekman-driven cross-slope motion analogous to that induced by flow–topography interactions. Importantly, the time mean is zero.

Figure 11b shows the resulting momentum balances for this experiment. Here, the circulation response takes the form of a persistent time-mean alternating jet structure over the slope (panel iii), with a prograde jet onshore and a retrograde jet offshore.

https://doi.org/10.5194/egusphere-2026-778
Preprint. Discussion started: 17 February 2026

This pattern is maintained by local convergence and divergence of momentum fluxes, which drive departures from the linear estimate at individual depths. The sign of these fluxes alternates across the slope, such that their contributions cancel in the domain integral. In this sense, the system permits local momentum redistribution and the formation of along-slope jets, but without corrugations there is no mechanism by which the oscillatory wind forcing can be converted into a net momentum transfer.

This flow structure can also be interpreted through the lens of potential vorticity rearrangement. Cross-slope motions driven by the time-variable wind induce local transport across the background PV gradient, leading to a redistribution of PV and the emergence of alternating along-slope jets. This pattern resembles jets associated with PV staircase formation (Dritschel and McIntyre, 2008), albeit without an explicit eddy field. Here, it is the wind forcing itself, rather than turbulent eddies, that mediates the cross-PV gradient transport.

5 Discussion

Previous realistic Arctic Ocean simulations have hinted that interactions between flow and topography may play an important role in shaping boundary currents around basins, as evidenced by two nonlinear features: a general prograde (cyclonic) offset of the flow strength relative to linear estimates, and an enhanced offset under anticyclonic wind forcing. Having now examined the underlying dynamics in an idealized setting, we can return to these features and consider what our results suggest about their expression in a more realistic setting.

A first consideration concerns the range of forcing timescales. In our simplified experiments, each forcing period produced a characteristic response; a short forcing period maintained a nearly steady prograde bias over the forcing period, whereas a long forcing period allowed partial relaxation toward the linear estimate and flow saturation during strong retrograde forcing. The transition to saturation, however, was found to depend mainly on flow strength, but with stronger forcing required to reach arrest under short-period forcing. In the realistic system, where surface stress varies continuously across frequencies and along the slope, these behaviors would coexist. Periods of slow, quasi-steady prograde forcing could permit relaxation, while energetic retrograde events could induce transient saturation. Together with along-slope variations in wind stress, such mixed conditions would produce a broader spectrum of circulation responses, helping to explain the spread seen in the realistic simulations (Fig. 1).

A second consideration relates to the topography. The slopes in our idealized experiments have a single dominant corrugation scale, whereas natural bathymetry spans a wide range of wavelengths and amplitudes. The arrest speed of topographic Rossby waves depends on their wavelength, so different topographic scales are associated with different arrest speeds and therefore result in saturation at different flow magnitudes. Fine-scale roughness is associated with short-wavelength waves that arrest at relatively weak retrograde flow, whereas broader features interact with longer waves that require stronger flow before arrest occurs. The resulting patchwork of local arrest conditions can be expected to smooth the sharp asymmetry found in our experiments, while retaining the same underlying nonlinear mechanism.

https://doi.org/10.5194/egusphere-2026-778
Preprint. Discussion started: 17 February 2026

Beyond differences in temporal and spatial scales, a realistic setting includes several processes absent from our simplified model, most notably stratification and vertical shear. Stratification is expected to alter the vertical structure of the response, tending to concentrate topographic interactions near the bottom, as found in stratified rectification studies (Brink, 2011). This suggests that the mechanism identified here may still operate, but with a depth-dependent signature.

Turning to implications for large-scale models, the mesoscale flow–topography interactions identified here require that the bathymetry is well-resolved. Thus, they may not be explicitly represented in coarse-resolution ocean models. In the context of Arctic circulation, this limitation becomes particularly relevant for future projections. Recent CMIP6 ensemble analyses indicate that surface stress over the Arctic Ocean is expected to intensify (Muilwijk et al., 2024), implying a stronger dynamical imprint of surface forcing on slope currents. As surface stress increases, the nonlinear mechanisms highlighted here are likely to play a larger role, meaning that coarse-resolution models may increasingly misrepresent the resulting boundary currents.

Finally, we have focused on a system where there is a local generation of eddies by flow–topography interactions. An open question is how additional sources of eddy activity, such as those arising from baroclinic instability, as well as remotely generated eddies entering the system, would influence the circulation. We hypothesize that a cyclonic bias will be established, where momentum is removed from the system by topographic form stress when eddies induce temporary retrograde flow over topographic irregularities. Related behavior has been documented in idealized studies, where an externally generated eddy field interacts with variable bathymetry, producing mean flows aligned with topography (Eurin, 1999). This question is particularly interesting in the context of a future "blue Arctic," where reduced sea-ice cover is projected to enhance eddy activity substantially (Li et al., 2024), potentially amplifying the role of eddy-topography interactions in shaping slope circulation.

6 Conclusions

This study examined the nonlinear dynamics of flow over corrugated slopes under time-variable forcing, and investigated how these interactions shape the relationship between circulation and surface forcing. The analysis was conducted in an idealized shallow-water model using two complementary frameworks – momentum budgets integrated along depth contours and along straight transects – which reveal how the same dynamics manifest themselves from different perspectives. We now return to the three questions posed in the introduction.

First, nonlinear flow–topography interactions introduce a systematic prograde bias in the circulation response. As the circulation strengthens, the retrograde flow reaches a critical velocity beyond which its strength saturates, while prograde flow can continue to increase, leading to a pronounced asymmetry between prograde and retrograde circulation. In the depth-following framework, both features originate from a net downslope flux of relative vorticity, which reaches its maximum during retrograde flow.

Second, the forcing period influences the persistence of this offset: rapid oscillations maintain an almost steady prograde bias, whereas slower forcing allows partial relaxation toward the linear response during prograde forcing phases. This behavior reflects the inertial low-pass filtering of the system combined with the net positive downslope vorticity flux, with its peak during retrograde flow. Saturation, however, depends primarily on flow strength; once retrograde flow arrests topographic

Rossby waves with wavelengths matching the along-slope topography, further acceleration is suppressed, resulting in saturation largely independent of timescale.

Third, the two diagnostic frameworks capture complementary aspects of the same process. In the depth-following framework, downslope vorticity fluxes quantify the nonlinear contribution and provide a clean diagnostic of the mechanisms driving the circulation offset and asymmetry. Importantly, we also show that topographic form stress does not necessarily vanish in this framework when integrated over an area (Eq. 26), even though it is zero along individual contours. In the momentum budget integrated along straight transects (which includes variations in depth), the same dynamics appear as a combination of momentum-flux convergence and topographic form stress, which represents a sink of momentum when integrated over the domain. In accordance with previous studies, form-stress closes the domain-integrated balance and clarifies why the net bias in circulation is prograde (Haidvogel and Brink, 1986; Brink, 2010).

Importantly, under quasi-geostrophic assumptions, these two perspectives can be unified as describing a flux of potential vorticity. In both frameworks, the residual time-mean prograde flow arises from a systematic flux of potential vorticity down the large-scale potential vorticity-gradient: in the presence of corrugations, flow–topography interactions generate topographic form stress that, through a chain of processes involving topographic Rossby wave dynamics, yield an integrated potential vorticity flux directed toward deeper water. When corrugations are absent, this mechanism vanishes and no net potential vorticity flux or residual flow is produced, consistent with the absence of form stress.

Overall, our results confirm that mesoscale topographic corrugations can induce a systematic prograde bias in time-variable slope currents and can sharply limit anticyclonic flow strength through Rossby wave arrest. The contribution of this study lies in examining how these nonlinear effects evolve with changing forcing, how they depend on the forcing period and strength, and how they can be interpreted consistently across diagnostic frameworks as a down-gradient PV flux (under QG scaling). Future work should examine how stratification, vertical shear, and externally generated eddies modify or reinforce this mechanism in more realistic settings.

Code and data availability. Code and data needed to reproduce the simulations, analysis and figures are available in a Zenodo repository (Sjur, 2026).

Appendix A: Additional figures

Figures A1 and A2 show the complete spatiotemporal evolution of the momentum-budget terms. Figure A1 show analysis on depth-contours, with terms defined in Eq. (11). Figure A2 show analysis on constant-y sections, with terms defined in Eq. (16).

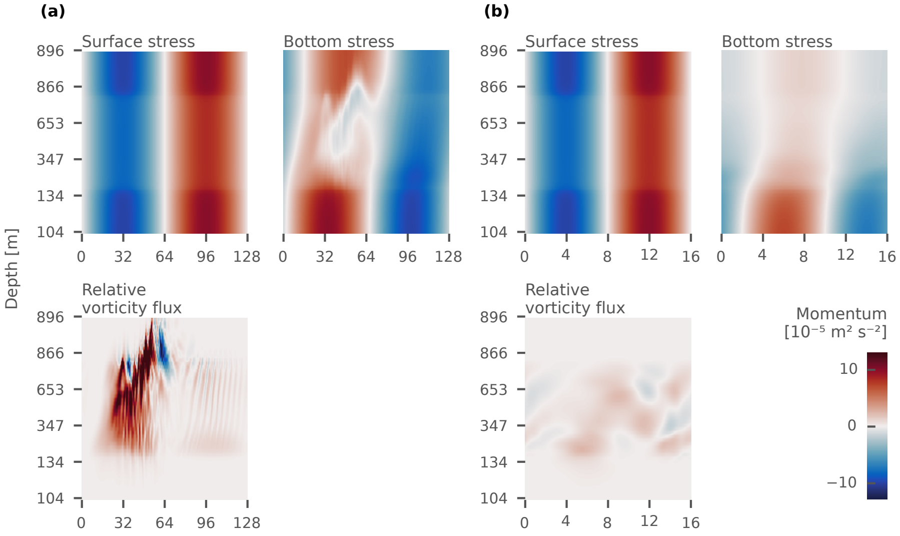

Figure A1. Hovmöller diagrams of momentum terms evaluated along depth-contours. Results for a forcing period of (a) 128 days, and (b) 16 days are shown. Each sub-figure displays surface stress, bottom stress (proportional to the circulation itself), and the nonlinear relative vorticity flux (positive offshore). The terms are defined in Eq. (11). Time is shown on the x-axis and depth the y-axis. Note that depth-contours are equally spaced in y, not in depth; the corresponding contours are shown in Fig. 2.

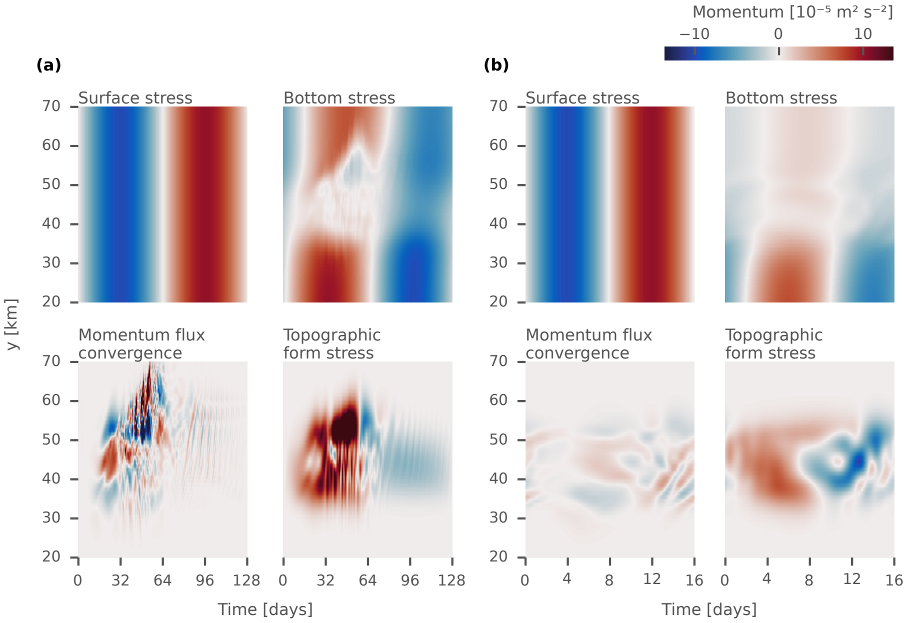

Figure A2. Hovmöller diagrams of momentum terms evaluated along constant-y sections. Results for a forcing period of (a) 128 days, and (b) 16 days are shown. Each sub-figure displays surface stress, bottom stress (proportional to the along-slope circulation), the convergence of nonlinear momentum flux, and the topographic form stress. The terms are defined in Eq. (16). Time is shown on the x-axis and cross-slope position y on the y-axis.

Appendix B: Additional derivations

B1 Amplitude of linear response to periodic forcing

We here derive the maximum amplitude of the solution to the linear depth following momentum equation (Eq. (11), retaining only linear terms) forced by the sinusoidal surface stress (Eq. (9)). The solution $U(H,t) = \overline{\boldsymbol{u}\cdot\boldsymbol{t}}^{H}$ satisfies

610 $$\partial_t U + (R/H)U = F(t)/H, \tag{B1}$$

where $F(t) = \overline{\boldsymbol{\tau}_s\cdot\boldsymbol{t}}^{H}$. For a purely zonal and spatially uniform stress $\tau_{sx}(t)\boldsymbol{i}$, the projection onto the contour reduces by the geometric factor $L_x/L_{C(H)}$, so that

$$F(t) = \frac{L_x}{L_{C(H)}}\tau_{sx}(t). \tag{B2}$$

Writing the surface stress in polar form, we have

615 $$\tau_{sx}(t) = \tau_0\sin(\omega t) = \Re\{-i\tau_0\, e^{i\omega t}\}, \tag{B3}$$

where $\Re\{\cdot\}$ is the real part. We seek a periodic solution of the form

$$U(H,t) = \Re\{\hat{u}(H)\,e^{i\omega t}\}. \tag{B4}$$

Substituting Eqs. (B3) and (B4) into Eq. (B1) gives the relation

$$\big(i\omega + R/H\big)\,\hat{u}(H) = \frac{L_x}{L_{C(H)}}\,\frac{-i\tau_0}{H}, \tag{B5}$$

620 and therefore

$$\hat{u}(H) = \frac{L_x}{L_{C(H)}}\,\frac{-i\tau_0/H}{(R/H)+i\omega}. \tag{B6}$$

Taking the magnitude yields

$$u_{\max}(H) = |\hat{u}(H)| = \frac{L_x}{L_{C(H)}}\,\frac{\tau_0}{H\sqrt{(R/H)^2+\omega^2}}. \tag{B7}$$

Factoring out R/H, we obtain the form used in Eq. (15) in the main text,

625 $$u_{\max}(H) = \frac{L_x}{L_{C(H)}}\,\frac{\tau_0}{R}\left[1+\left(\frac{\omega H}{R}\right)^2\right]^{-1/2}. \tag{B8}$$

Author contributions. ALPS and PEI designed the experimental framework. ALPS implemented the experiments, carried out the simulations and analyses, and produced the figures. All authors contributed to the theoretical development and interpretation of results. ALPS prepared the original manuscript, and all authors revised and approved the final version.

Competing interests. The authors declare that they have no competing interests.

630 *Acknowledgements.* This work was supported by the Research Council of Norway through the TopArctic project (grant 314826). We thank Kenneth Brink for making the coastal trapped-wave code publicly available. AI tools have been used exclusively for language editing and coding support; all scientific analysis, data processing, interpretation, and conclusions were carried out by the authors.

References

Bai, Y., Wang, Y., and Stewart, A. L.: Does Topographic Form Stress Impede Prograde Ocean Currents?, Journal of Physical Oceanography, 51, 2617–2638, https://doi.org/10.1175/JPO-D-20-0189.1, number: 8, 2021.

Boyer, D. L., Zhang, X., and Pérenne, N.: Laboratory observations of rotating, stratified flow in the vicinity of a submarine canyon, Dynamics of Atmospheres and Oceans, 31, 47–72, https://doi.org/10.1016/S0377-0265(99)00028-7, 2000.

Bretherton, F. P. and Haidvogel, D. B.: Two-dimensional turbulence above topography, Journal of Fluid Mechanics, 78, 129–154, https://doi.org/10.1017/S002211207600236X, 1976.

Brink, K. H.: Topographic Drag Due to Barotropic Flow over the Continental Shelf and Slope, Journal of Physical Oceanography, 16, 2150–2158, https://doi.org/10.1175/1520-0485(1986)016<2150:TDDTBF>2.0.CO;2, 1986.

Brink, K. H.: Topographic rectification in a forced, dissipative, barotropic ocean, Journal of Marine Research, 68, 337–368, https://doi.org/10.1357/002224010794657209, number: 3-4, 2010.

Brink, K. H.: Topographic rectification in a stratified ocean, Journal of Marine Research, 69, 483–499, https://doi.org/10.1357/002224011799849354, 2011.

Brink, K. H.: Stable barotropic coastal trapped wave modes: edge, shelf and Kelvin waves (Version 3), MATLAB code package, Woods Hole Oceanographic Institution, available at: https://hdl.handle.net/1912/26311.3, 2025.

Broomé, S. and Nilsson, J.: Stationary Sea Surface Height Anomalies in Cyclonic Boundary Currents: Conservation of Potential Vorticity and Deviations from Strict Topographic Steering, Journal of Physical Oceanography, 46, 2437–2456, https://doi.org/10.1175/JPO-D-15-0219.1, 2016.

Constantinou, N. C. and Young, W. R.: Beta-plane turbulence above monoscale topography, Journal of Fluid Mechanics, 827, 415–447, https://doi.org/10.1017/jfm.2017.482, 2017.

Dritschel, D. G. and McIntyre, M. E.: Multiple Jets as PV Staircases: The Phillips Effect and the Resilience of Eddy-Transport Barriers, Journal of the Atmospheric Sciences, https://doi.org/10.1175/2007JAS2227.1, 2008.

Eurin, D.: Circulation and cross-shelf exchanges over an irregular coastal topography, Ph.D. thesis, University of British Columbia, https://doi.org/10.14288/1.0053157, 1999.

Gill, A. E.: Atmosphere–Ocean Dynamics, no. 30 in International Geophysics Series, Academic Press, San Diego, ISBN 0-12-283522-0, 1982.

Haidvogel, D. B. and Brink, K. H.: Mean Currents Driven by Topographic Drag over the Continental Shelf and Slope, Journal of Physical Oceanography, 16, 2159–2171, https://doi.org/10.1175/1520-0485(1986)016<2159:MCDBTD>2.0.CO;2, 1986.

Holloway, G.: Systematic forcing of large-scale geophysical flows by eddy-topography interaction, Journal of Fluid Mechanics, 184, 463–476, https://doi.org/10.1017/S0022112087002970, 1987.

Holloway, G.: Neptune effect: statistical mechanical forcing of ocean circulation, in: Stochastic Modelling in Physical Oceanography, edited by Adler, R. J., Müller, P., and Rozovskii, B. L., pp. 207–219, Birkhäuser Boston, Boston, MA, ISBN 978-1-4612-7533-6 978-1-4612-2430-3, https://doi.org/10.1007/978-1-4612-2430-3_8, 1996.

Isachsen, P. E., LaCasce, J. H., Mauritzen, C., and Häkkinen, S.: Wind-Driven Variability of the Large-Scale Recirculating Flow in the Nordic Seas and Arctic Ocean, Journal of Physical Oceanography, 33, 2534–2550, https://doi.org/10.1175/1520-0485(2003)033<2534:WVOTLR>2.0.CO;2, 2003.

https://doi.org/10.5194/egusphere-2026-778
Preprint. Discussion started: 17 February 2026

Johnston, T. M. S., Sjur, A. L. P., Isachsen, P. E., and LaCasce, J. H.: Eddy- and Wind-Driven Circulation in the Enclosed Basins of the Norwegian Sea Evaluated Using a Model and Absolute Geostrophic Flow From Argo, Journal of Geophysical Research: Oceans, 130, e2024JC021 990, https://doi.org/10.1029/2024JC021990, 2025.

Kallmyr, J.-A. H., Nilsson, J., Chafik, L., and Isachsen, P. E.: The Time-Mean Arctic Ocean Circulation as Seen Through Satellite Altimetry and Hydrography, Journal of Geophysical Research: Oceans, 130, e2024JC022 203, https://doi.org/10.1029/2024JC022203, 2025.

Li, X., Wang, Q., Danilov, S., Koldunov, N., Liu, C., Müller, V., Sidorenko, D., and Jung, T.: Eddy activity in the Arctic Ocean projected to surge in a warming world, Nature Climate Change, 14, 156–162, https://doi.org/10.1038/s41558-023-01908-w, publisher: Nature Publishing Group, 2024.

Masich, J., Chereskin, T. K., and Mazloff, M. R.: Topographic form stress in the Southern Ocean State Estimate, Journal of Geophysical Research: Oceans, 120, 7919–7933, https://doi.org/10.1002/2015JC011143, 2015.

Muilwijk, M., Hattermann, T., Martin, T., and Granskog, M. A.: Future sea ice weakening amplifies wind-driven trends in surface stress and Arctic Ocean spin-up, Nature Communications, 15, 6889, https://doi.org/10.1038/s41467-024-50874-0, 2024.

Munk, W. H. and Palmén, E.: Note on the Dynamics of the Antarctic Circumpolar Current, Tellus A: Dynamic Meteorology and Oceanography, 3, https://doi.org/10.3402/tellusa.v3i1.8609, 1951.

Nilsson, J., Kallmyr, J.-A. H., and Isachsen, P. E.: Topographic Steering of the Upper Arctic Ocean Circulation by Deep Flows, Tellus A: Dynamic Meteorology and Oceanography, 76, 206–226, https://doi.org/10.16993/tellusa.4072, 2024.

Nøst, O. A. and Isachsen, P. E.: The large-scale time-mean ocean circulation in the Nordic Seas and Arctic Ocean estimated from simplified dynamics, Journal of Marine Research, 61, 175–210, https://doi.org/10.1357/002224003322005069, 2003.

Salmon, R., Holloway, G., and Hendershott, M. C.: The equilibrium statistical mechanics of simple quasi-geostrophic models, Journal of Fluid Mechanics, 75, 691–703, https://doi.org/10.1017/S0022112076000463, 1976.

Samelson, R. M. and Allen, J. S.: Quasi-Geostrophic Topographically Generated Mean Flow over the Continental Margin, Journal of Physical Oceanography, 17, 2043–2064, https://doi.org/10.1175/1520-0485(1987)017<2043:QGTGMF>2.0.CO;2, 1987.

Sjur, A. L. P.: alpsjur/temporal-topo-flow: v1.0.0, https://doi.org/10.5281/zenodo.18494674, 2026.

Sjur, A. L. P., Isachsen, P. E., Nilsson, J., LaCasce, J. H., and Ryseth, M. D.: The Wind-Driven Time-Variable Circulation in the Arctic Mediterranean, Journal of Geophysical Research: Oceans, 130, e2024JC021 713, https://doi.org/10.1029/2024JC021713, 2025.

Stevens, D. P. and Ivchenko, V. O.: The zonal momentum balance in an eddy-resolving general-circulation model of the southern ocean, Quarterly Journal of the Royal Meteorological Society, 123, 929–951, https://doi.org/10.1002/qj.49712354008, 1997.

Stewart, A. L. and Hogg, A. M.: Reshaping the Antarctic Circumpolar Current via Antarctic Bottom Water Export, Journal of Physical Oceanography, 47, 2577–2601, https://doi.org/10.1175/JPO-D-17-0007.1, 2017.

Timmermans, M. and Marshall, J.: Understanding Arctic Ocean Circulation: A Review of Ocean Dynamics in a Changing Climate, Journal of Geophysical Research: Oceans, 125, e2018JC014 378, https://doi.org/10.1029/2018JC014378, 2020.

Wagner, G. L., Silvestri, S., Constantinou, N. C., Ramadhan, A., Campin, J.-M., Hill, C., Chor, T., Strong-Wright, J., Lee, X. K., Poulin, F., Souza, A., Burns, K. J., Marshall, J., and Ferrari, R.: High-level, high-resolution ocean modeling at all scales with Oceananigans, https://arxiv.org/abs/2502.14148, 2025.

Ward, M. L. and Hogg, A. M.: Establishment of momentum balance by form stress in a wind-driven channel, Ocean Modelling, 40, 133–146, https://doi.org/10.1016/j.ocemod.2011.08.004, 2011.

Woodgate, R.: Arctic Ocean Circulation: Going Around at the Top of the World, Nature Education Knowledge, 4, 8, https://www.nature.com/scitable/knowledge/library/arctic-ocean-circulation-going-around-at-the-102811553/, 2013.

Woodgate, R. A., Aagaard, K., Muench, R. D., Gunn, J., Björk, G., Rudels, B., Roach, A. T., and Schauer, U.: The Arctic Ocean Boundary Current along the Eurasian slope and the adjacent Lomonosov Ridge: Water mass properties, transports and transformations from moored instruments, Deep Sea Research Part I: Oceanographic Research Papers, 48, 1757–1792, https://doi.org/10.1016/S0967-0637(00)00091-1, 2001.

Yang, J., Proshutinsky, A., and Lin, X.: Dynamics of an idealized Beaufort Gyre: 1. The effect of a small beta and lack of western boundaries, Journal of Geophysical Research: Oceans, 121, 1249–1261, https://doi.org/10.1002/2015JC011296, 2016.

Zhang, W. and Lentz, S. J.: Wind-Driven Circulation in a Shelf Valley. Part I: Mechanism of the Asymmetrical Response to Along-Shelf Winds in Opposite Directions, Journal of Physical Oceanography, https://doi.org/10.1175/JPO-D-17-0083.1, 2017.

Zhang, X., Boyer, D. L., Pérenne, N., and Renouard, D. P.: Mean flow generation along a sloping region in a rotating homogeneous fluid, Journal of Geophysical Research: Oceans, 101, 28 597–28 614, https://doi.org/10.1029/96JC02834, 1996.